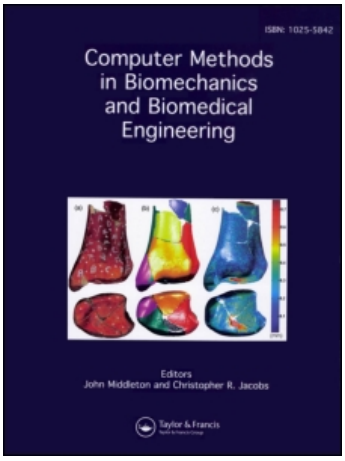

Computer Methods in Biomechanics and Biomedical Engineering
Publication details, including instructions for authors and subscription information:
http://www.informaworld.com/smpp/title~content=t713455284

Mechanics and electrostatics of the interactions between osteoblasts and titanium surface

D. Kabaso[a]; E. Gongadze[b]; Š. Perutková[a]; C. Matschegewski[c]; V. Kralj-Iglič[d]; U. Beck[b]; U. van Rienen[b]; A. Iglič[a]
[a] Laboratory of Biophysics, Faculty of Electrical Engineering, University of Ljubljana, Ljubljana, Slovenia [b] Faculty of Computer Science and Electrical Engineering, University of Rostock, Rostock, Germany [c] Department of Cell Biology, Biomedical Research Centre, Medical Faculty, University of Rostock, Rostock, Germany [d] Laboratory of Clinical Biophysics, Faculty of Medicine, University of Ljubljana, Ljubljana, Slovenia

Online publication date: 21 April 2011

To cite this Article Kabaso, D. , Gongadze, E. , Perutková, Š. , Matschegewski, C. , Kralj-Iglič, V. , Beck, U. , van Rienen, U. and Iglič, A.(2011) 'Mechanics and electrostatics of the interactions between osteoblasts and titanium surface', Computer Methods in Biomechanics and Biomedical Engineering, 14: 5, 469 — 482
To link to this Article: DOI: 10.1080/10255842.2010.534986
URL: http://dx.doi.org/10.1080/10255842.2010.534986

Computer Methods in Biomechanics and Biomedical Engineering
Vol. 14, No. 5, May 2011, 469–482

Taylor & Francis
Taylor & Francis Group

Mechanics and electrostatics of the interactions between osteoblasts and titanium surface

D. Kabaso[a], E. Gongadze[b], Š. Perutková[a], C. Matschegewski[c], V. Kralj-Iglič[d], U. Beck[b], U. van Rienen[b] and A. Iglič[a]*

[a]*Laboratory of Biophysics, Faculty of Electrical Engineering, University of Ljubljana, Ljubljana, Slovenia;* [b]*Faculty of Computer Science and Electrical Engineering, University of Rostock, Rostock, Germany;* [c]*Department of Cell Biology, Biomedical Research Centre, Medical Faculty, University of Rostock, Rostock, Germany;* [d]*Laboratory of Clinical Biophysics, Faculty of Medicine, University of Ljubljana, Ljubljana, Slovenia*

(*Received 31 July 2010; final version received 22 October 2010*)

Due to oxidation and adsorption of chloride and hydroxyl anions, the surface of titanium (Ti) implants is negatively charged. A possible mechanism of the attractive interaction between the negatively charged Ti surface and the negatively charged osteoblasts is described theoretically. It is shown that adhesion of positively charged proteins with internal charge distribution may give rise to attractive interaction between the Ti surface and the osteoblast membrane. A dynamic model of the osteoblast attachment is presented in order to study the impact of geometrically structured Ti surfaces on the osteoblasts attachment. It is indicated that membrane-bound protein complexes (PCs) may increase the membrane protrusion growth between the osteoblast and the grooves on titanium (Ti) surface and thereby facilitate the adhesion of osteoblasts to the Ti surface. On the other hand, strong local adhesion due to electrostatic forces may locally trap the osteoblast membrane and hinder the further spreading of osteointegration boundary. We suggest that the synergy between these two processes is responsible for successful osteointegration along the titanium surface implant.

Keywords: osteoblast; cell attachment; membrane electrostatics; microstructures; protein-mediated interactions; titanium implants

1. Introduction

Interactions between the implant surface and the surrounding bone tissue are essential for the successful integration of a bone implant. Due to its good biocompatibility, titanium (Ti) and its alloys (Cai et al. 2006) are being widely used in a variety of orthopaedic and dental implantations.

The oxide layer, naturally formed on it, is thought to be mainly responsible for its good biocompatible behaviour (Roessler et al. 2002). This oxidation and the dissolution of metal cations (Butt et al. 2003) partially yield to a negative surface potential, i.e. negative surface charge density of Ti implants. In addition, the negative surface potential is a consequence of a preferential adsorption of chloride and hydroxyl anions incorporated in the structure of the TiO_2 layer (Roessler et al. 2002; Monsees et al. 2005). We should note that a contribution to the negative surface potential would have as well an applied voltage to the electrostimulative implants (Butt et al. 2003). The negatively charged surface of the Ti implant attracts cations and repels anions, and consequently an electric double layer is formed (Gouy 1910; Chapman 1913; Roessler et al. 2002; Cai et al. 2006). Therefore, the surface potential strongly depends on the surrounding ionic strength (Roessler et al. 2002).

The adhesion of osteoblasts to the Ti surface is a prerequisite for the successful osteointegration of the implant (Monsees et al. 2005). It was suggested that the contact between the cell membrane of osteoblasts and the Ti oxide surface is established in two steps (Walboomers and Jansen 2001; Monsees et al. 2005). Firstly, the osteoblast's cell membrane makes a non-specific contact due to electrostatics, followed by a second step, where the specific binding takes place. Many studies in the past have shown that the negative surface potential of Ti implants promotes osteoblast adhesion and consequently the new bone formation (Teng et al. 2000; Oghaki et al. 2001; Smeets et al. 2009). Since osteoblasts are negatively charged (Smeets et al. 2009), they would be electrostatically repelled by the negatively charged Ti surface if some other attractive forces would not be present in the system. Therefore, recently a mechanism of osteoblast binding to the implant surface was proposed assuming that positively charged proteins, attached to the negatively charged implant surface, serve as a substrate for the subsequent attachment of the osteoblasts (Smith et al. 2004; Smeets et al. 2009). The aim of this work is to clarify the physical mechanism underlying the charged protein-mediated attractive interaction between the negatively charged osteoblast membrane and the negatively charged Ti implant surface. Furthermore, to determine whether the contributions of membrane-bound

*Corresponding author. Email: ales.iglic@fe.uni-lj.si

ISSN 1025-5842 print/ISSN 1476-8259 online

DOI: 10.1080/10255842.2010.534986
http://www.informaworld.com

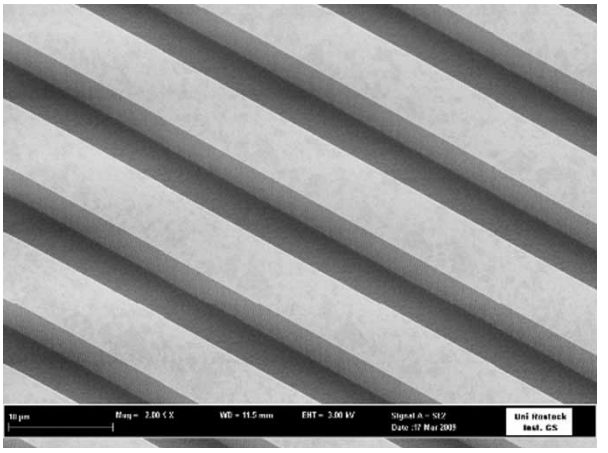

Figure 1. Rectangular profiles coated with 50-nm titanium.

protein complexes (PCs) to the membrane's free energy could explain the puzzling experimental data demonstrating no osteointegration between the narrow grooves and considerable osteointegration between the wide grooves of Ti surface implants (Puckett et al. 2008; Lange et al. 2009; Lamers et al. 2010; Matschegewski et al. 2010) (Figure 1).

2. Monte Carlo simulation of distribution and orientation of proteins (macro-ions) near charged Ti surface

In accordance with previous suggestions (Smith et al. 2004; Smeets et al. 2009), we assume that the initial attractive interaction between the negatively charged Ti surface and the negatively charged osteoblast membrane surface is mediated by the adhesion of positive macro-ions (proteins) with internal charge distribution. This adhesion originates in Coulomb interaction between the negatively charged surface and positively charge proteins. In our theoretical model, the single spheroidal protein is composed of two positive charges (each of the valency Z_s), separated by a distance D equal to the length of the protein along its axis (see Figures 2 and 3).

In order to predict the orientation of such proteins near a charged implant surface, we performed the Monte Carlo (MC) simulations of the distribution and the orientation

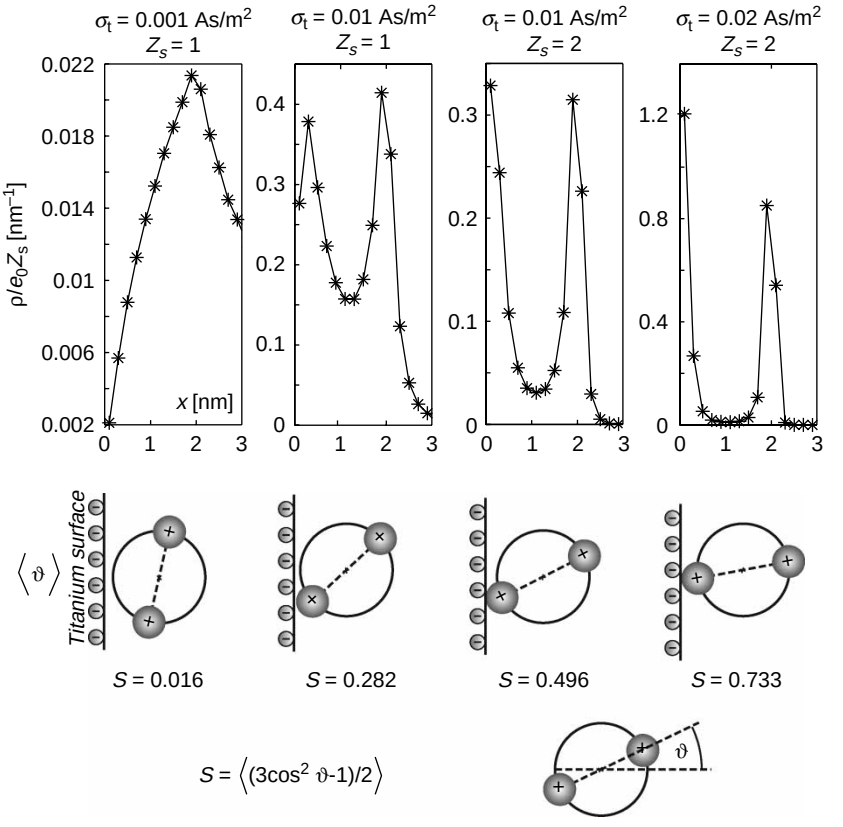

Figure 2. Volume charge density of divalent macro-ions (ρ) dependent on the distance from the charged surface for different values of the area charge density on the planar surface σ_t and two different valencies $Z_s = 1$ and 2. The values of the average order parameter S computed for the slice of $x = (0, 1.25)$ nm in the closest vicinity of the charged surface are added under each graph, where S is schematically described below. The average orientational angle of the macro-ions is also shown schematically.

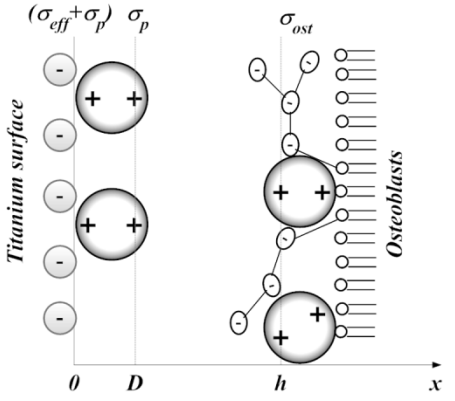

Figure 3. Schematic figure of a charged titanium implant surface and a charged osteoblast's surface, interacting in an electrolyte solution. The effective surface charge density of the implant surface is σ_{eff}, while the effective surface charge density of the osteoblast surface is σ_{ost}. Due to the bound positively charged macroions with internal charge distribution, the surface charge distribution of the Ti surface is described by two surface charge densities $\sigma_{\text{eff}} + \sigma_{\text{p}}$ and σ_{p}.

of charged spherical proteins in the close vicinity of the charged planar surface with the surface charge density σ_{t}. The simulation system consisted of a box with a volume Y^2L, where Y^2 is the area of both planar surfaces that confine the system and $L = 10\,\text{nm}$ is the distance between these two surfaces. We assume that electric field changes just along x-axis, which is perpendicular to the charged surfaces, i.e. along the length L. Within the box, 200 spherical proteins with internal charge distribution are included (Figure 2) having a diameter $D = 2\,\text{nm}$. The hard-core interactions between the proteins and the charged surfaces of implant are taken into account by means of the distance of the closest approach (Urbanija et al. 2008; Perutkova, Frank et al. 2010). For the sake of simplicity, the hard core interactions between the proteins are neglected. The distance between the charged planar surfaces (L) is chosen to be long enough not to effect the protein distribution close to the charged surface. The system is canonical and the condition of electroneutrality is kept in our MC simulation. The periodic boundary conditions are used in the same way as in the work of Moreira and Netz (2002). In each step of MC simulation, one protein was chosen randomly and was randomly linearly shifted or rotated. The probability of the selection of the type of the move (rotation or translation) is equal (Frenkel and Smith 2002). The run time was around 2×10^7 steps for the whole system of particles and the MC evaluation starts after the thermodynamic equilibrium of the system is reached.

The MC simulations provided the volume charge density profile (ρ) of the protein charges in the vicinity of the Ti surface and the average order parameter $S = \langle(3\cos^2\vartheta - 1)/2\rangle$ within 1.25-nm wide slice, where ϑ is the angle between the protein axis and the horizontal x-axis. The two point charges (with valency Z_{s}) within a single protein are supposed to be indistinguishable; thus, the angles ϑ and $(\vartheta + \pi)$ are treated equally, see Figure 2. $S = 0$ means that proteins are not oriented at all, while $S = 1$ indicates that proteins are fully oriented along the x-axis perpendicular to the charged surface. The simulations were performed for different values of surface charge density of Ti surface (σ_{t}) and for different valencies of the single ion within the spherical protein with internal charge distribution (Z_{s}). The calculated volume charge density ρ (Figure 2) shows that for smaller values of σ_{t}, there appears only one small distribution peak which indicates that the proteins are concentrated close to the surface without any orientation and also the concentration is low. On the other hand, for higher values of σ_{t}, there are two peaks indicating stronger orientation of the macroions and their high concentration near the wall. Moreover, for high enough values of σ_{t} and Z_{s}, the concentration of the ions away from the Ti surface is zero. It can be seen that proteins are more oriented for higher values of the surface charge density of the charged surface and for the higher values of the valency Z_{s}. Based on the results presented in Figure 2, it can be concluded that for higher surface charge densities of Ti surface, the adhered proteins with internal charge distribution would be nearly completely oriented as schematically shown in Figure 3.

3. On the origin of attractive interaction between osteoblast and Ti surface

In the model, the solution of the electrolyte (NaCl) and charged proteins occupy the space between two planar charged surfaces (Ti implant surface and osteoblast surface) with effective surface charge densities σ_{eff} and σ_{ost}, respectively.

Based on the results presented in the previous section (Figure 2), we assume that the adhered proteins with internal charge distribution are fully oriented (Figure 3). In accordance, the positive charge of the tips of bound proteins is represented by a charged surface (with the surface charge density σ_{p}) at a distance D from the Ti surface (Figure 3). Due to the second charge of the bound proteins, the surface charge density of the Ti surface is reduced to the value $(\sigma_{\text{eff}} - \sigma_{\text{p}})$.

The lipid bilayer of the osteoblasts' membrane is covered by a thick layer of charged glycoproteins with more or less homogeneous volume distribution of its negative electric charge as schematically shown in Figure 3. In our model, we assume that spheroidal charged proteins with internal charged distribution are embedded also in glycoprotein layer. However, since these proteins are surrounded by homogeneously distributed negative charge of glycoproteins and since the charge of lipid head

groups in the outer lipid layer is negligible (see Iglič et al. 1997 and references therein), these proteins are not preferentially oriented. For the sake of simplicity in this work, the total charge distribution of negatively charged glycoprotein layer together with positively charged embedded proteins is described by effective surface charge density σ_{ost} (Figure 3).

In order to determine the electric potential in the system, we solve Poisson–Boltzmann Equation (see, for example, Cevc 1990; Safran 1994; Israelachvili 1997):

$$\frac{d^2\Psi(x)}{dx^2} = \kappa^2 \sinh(\Psi(x)), \tag{1}$$

where we introduce the reduced electrostatic potential $\Psi = e_0\phi/kT$ and Debye length $l_D = \kappa^{-1} = \sqrt{\epsilon\epsilon_0 kT/2n_0e_0^2}$. Here $\phi(x)$ is the electrostatic potential, e_0 is the elementary charge, kT is the thermal energy, ϵ is the permittivity of water, ϵ_0 is the permittivity the free space and n_0 is the bulk number density of positively and negatively charged ions in electrolyte solution. The axis x is perpendicular to the implant surface and points in the direction of bulk solution. We assume the electroneutrality of the whole system and that the electrostatic field varies only in the normal direction between the two charged surfaces (i.e. in x-direction). The bulk solution (outside the space between both charged surfaces) provides a suitable reference for the electric potential (i.e. $\Psi = 0$). The condition of electroneutrality of the system is in agreement with the boundary conditions:

$$\frac{d\Psi}{dx}(x = 0) = -(\sigma_{eff} + \sigma_p)\, e_0/\epsilon\epsilon_0 kT, \tag{2}$$

$$\Psi(x = D_-) = \Psi(x = D_+), \tag{3}$$

$$\frac{d\Psi}{dx}(x = D_-) = \frac{d\Psi}{dx}(x = D_+) + \sigma_p\, e_0/\epsilon\epsilon_0 kT, \tag{4}$$

$$\frac{d\Psi}{dx}(x = h) = \sigma_{ost}\, e_0/\epsilon\epsilon_0 kT. \tag{5}$$

The free energy of the system per unit area surface A is characterised by the energy stored in the electrostatic field (first term) and entropic contribution of salt ions (second term) (see, for example, Bohinc et al. 2008):

$$F/A = \int_0^h \left(\frac{1}{2}\epsilon\epsilon_0 \left(\frac{d\Psi}{dx}\frac{kT}{e_0} \right)^2 + kT \sum_{i=+,-} \left(n_j \ln\left(\frac{n_j}{n_0}\right) - (n_j - n_0) \right) \right) dx, \tag{6}$$

where n_j are the number densities of anions ($i = -$) and cations ($i = +$) in the salt solution.

Figure 4 shows the dependency of the free energy of the system (F) on the distance h for different values of the surface charge density σ_p attributed to the bound divalent proteins. Inset in Figure 4 shows the case of $\sigma_p = 0$, where the attached positively charged proteins are not present in the system; therefore, the free energy F strongly increases with decreasing distance h corresponding to strong repulsive force between like-charged Ti and osteoblast surfaces. Since $\sigma_p = 0$, there are no attached proteins on Ti surface, there is also no steric restriction for osteoblast surface which is, therefore, free to approach to Ti surface at a distance $h = 0$. On the other hand, for $\sigma_p > 0$, the proteins bound to Ti surface prevent the closest approach of osteoblasts to Ti surface so that $h \geq D$ (see also Figure 3). It can be seen in Figure 4 that, for $\sigma_p > 0$, the free energy decreases with decreasing h until the absolute minimum of F close to $h \cong D$ is reached. It can be, therefore, concluded that at large enough D and σ_p, the attached positively charged proteins with internal charge distribution can turn the repulsive force between the negatively charged Ti and the osteoblast surfaces into attractive force.

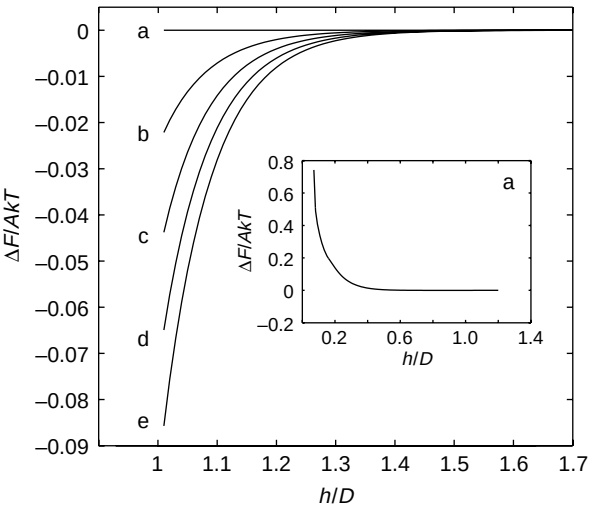

Figure 4. Free energy $\Delta F = F - F(h \to \infty)$ (in the units of AkT) as a function of h/D for different values of σ_p : 0 As/m^2 (a), 0.002 As/m^2 (b), 0.004 As/m^2 (c), 0.006 As/m^2 (d) and 0.008 As/m^2 (e). Inset: the dependence of ΔF for $\sigma_p = 0$, steric restriction due to attached proteins is not taken into account. Length of the attached proteins $D = 10$ nm. Values of other model parameters are $\sigma_{eff} = -0.4$ As/m^2, $\sigma_{ost} = -0.05$ As/m^2, salt concentration in the bulk solution $n_0/N_A = 150$ mmol/l, where N_A is Avogadro's number.

The results presented in Figure 4 reflect the fact that two adjacent negatively charged surfaces (Ti surface and osteoblast surface) without bound positively charged proteins repel each other, while for high enough concentration of bound positively charged proteins with internal charge distribution, the force between two negatively charged surfaces becomes strongly attractive leading to the equilibrium distance at $h \cong D$ (Figure 5).

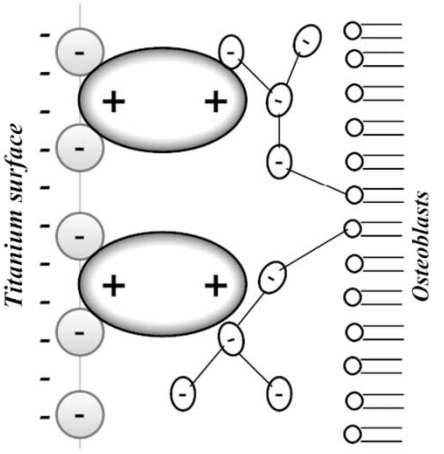

Figure 5. Schematic figure of orientation of the positively charged proteins (with internal charge distribution) bound to Ti surface at an equilibrium distance between the charged implant surface and the charged osteoblast's surface.

The origin of attractive interactions between the two negatively charged surfaces is the electrostatic attraction between the positively charged domain on the tip of the Ti surface-bound protein and the negatively charged opposite membrane of osteoblast (Figure 5).

4. The influence of Ti surface topography on osteointegration

The osteointegration on Ti implants depends on the Ti topographical characteristics. The present biomechanical study assumes that membrane-bound PCs with a negative intrinsic curvature reduce the effective membrane surface tension allowing membrane growth in Ti surface grooves (Figure 7). The binding of osteoblasts to the Ti surface reduces the free energy of the system. On the other hand, the strong interactions at contact regions trap the membrane, thereby increasing the local lateral membrane tension resulting in increase in free energy of the cell membrane. In this study, we show that the cost of bending energy to protrude many narrow grooves is higher than the cost to protrude a single wide groove of the same total length. We suggest that the balance between the cost of bending energy and the gain in adhesion energy may explain experimental results in which osteoblasts fail to grow in narrow grooves, while growth is increased in wider grooves (Puckett et al. 2008; Lange et al. 2009; Lamers et al. 2010; Matschegewski et al. 2010).

The present model suggests that the facilitated growth in wide grooves along the Ti surface is due to PCs with negative curvature inducing domain (Iglič et al. 2006; Zimmerberg and Kozlov 2006; Iglič, Lokar et al. 2007). Recent experimental studies have implicated Bin/Amphiphysin/Rvs (BAR) and IRSp53-missing in metastasis (IMD) protein domains as responsible for sensing and inducing concave and convex curvatures, respectively (Peter et al. 2004; Mattila et al. 2007). The BAR and IMD protein domain structures have a crescent-shaped dimer which binds preferentially to curved membranes (Shlomovitz and Gov 2008), and these domains have also been shown to tubulate membranes (Zimmerberg and Kozlov 2006; Iglič, Slivnik et al. 2007; Shlomovitz and Gov 2008; Perutkova, Kralj-Iglič et al. 2010). In some of the previous theoretical studies, it was shown how such crescent-shaped proteins may induce the spontaneous initiation of tubular membrane protrusions (Iglič et al. 2006; Zimmerberg and Kozlov 2006; Veksler and Gov 2007; Sorre et al. 2009; Perutkova, Kralj-Iglič et al. 2010).

In recent studies, it has been shown that adhesion molecules such as integrin connect the cell membrane to the external substrate and due to their negative binding energy, they reduce the membrane surface tension (Engler et al. 2004; Discher et al. 2005). This binding to the external substrate sends a transmembrane signal, since the adhesion molecules are also linked to the actomyosin cytoskeleton (Discher et al. 2005). Whereas other studies demonstrated that cells grow focal adhesions from their corner regions of convex curvature (defined as the outwards normal vector) (Brock et al. 2003). Therefore, we hypothesise that PCs (e.g. adhesion molecules) at the contact regions between the osteoblast membrane and the Ti surface have a negative intrinsic spontaneous curvature (e.g. IRSp53), and due to the mismatch with the membrane curvature, they initiate protrusive forces leading to osteointegration along Ti implants.

4.1 The model

The basic equations of motion of the membrane contour and the time dependence of non-stable lateral density of membrane PCs are derived first. We then perform a linear stability analysis for the nearly flat membrane shape.

The shapes explored in this model describe a segment of the cell outer contour, where the membrane is initially flat (Figure 6). This geometry can also be used for a flat 2D membrane, under the constraint of translational symmetry. Here, we need to pin the membrane using an external force to prevent its drifting motion. This external force mimics the effects of the restoring forces due to the adhesion of the rest of the cell to the Ti surface. In addition, we assume that the membrane curvature in a perpendicular direction along the contour is roughly constant (Figure 6(A)), and thus, it enters our calculation as a modified membrane tension. More specifically, if the osteoblast cell is on the top of the Ti surface, we only take into account a segment of the contour in contact with the Ti surface (Figure 7(A)). Regarding the PCs in our model, we assume that their overall number on the membrane is conserved, and that they are allowed to move along the osteoblast membrane.

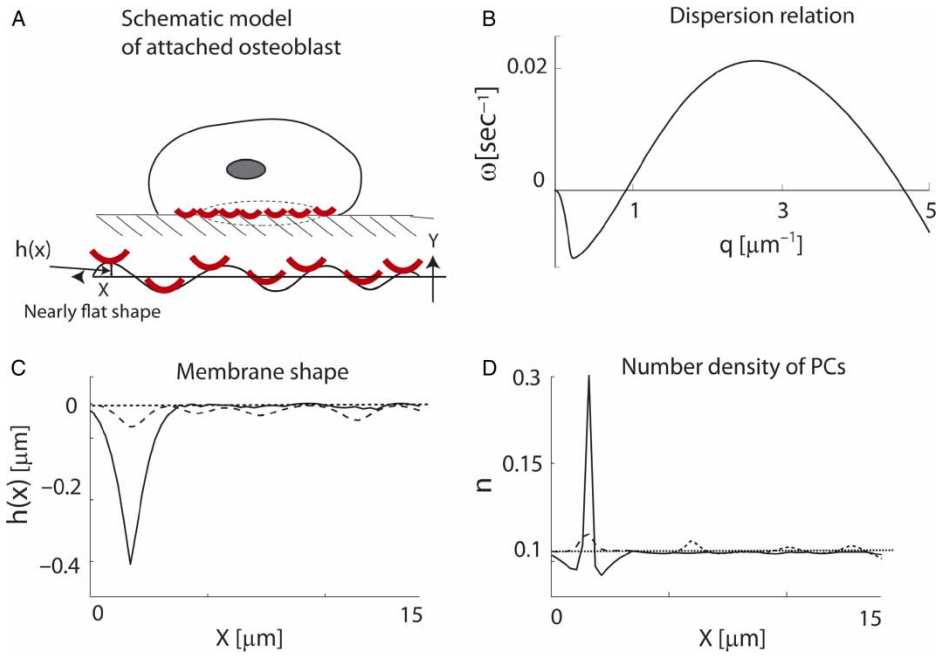

Figure 6. The dispersion relation describing the dynamical instability of membrane protrusion growth. (A) Schematic model of the flat membrane shape. The membrane shape is modelled as a 1D contour in the (x,y) coordinate system (with a constant strip width), which describes a contour of membrane segment from an elliptical osteoblast in the XY projection. The crescent-shaped curves are illustrations of the PCs with negative curvature, which is the curvature at the tip of protrusions. The PCs are adhesion molecules with negative intrinsic curvature, $\bar{H} = -10\,\mu\text{m}^{-1}$. Denote that $h(x)$ describes the small deformations from the flat-shaped membrane. (B) The wavelength $w(q)$ is a function of different wavevectors q. Each wavevector equals $2\pi/\lambda$. Note that the positive values of $w(q)$ describe non-stable regions while the negative values of $w(q)$ describe stable regions. (C) Membrane dynamics driven by small and random perturbations in the density of adhesion molecules. Initially, the membrane shape is flat (dotted line). At intermediate time (150 s), the membrane dynamics shows a rapid growth of four waves (dashed line), which matches the fastest wave vector of $2.5\,\mu\text{m}^{-1}$ according to the dispersion relation in (B). At steady state (300 s), the four membrane protrusions are coalesced into a single protrusion (solid line). (D) The distribution of adhesion molecules (n) is according to the membrane shape dynamics. Initially, a small ($<1\%$) and random noise in the density of molecules is added to the initial uniform distribution of molecules (dotted line). The four-peak distributions at intermediate time (dashed line) are then coalesced into a single peak distribution at steady state time (solid line).

4.2 *Equations of motion*

Our model investigates the coupling between the adhesion of osteoblast cells and the membrane curvature. We give below the free energy expression used in the model, from which we derive the equations of motion of the membrane contour and density distribution.

The continuum free energy in our model is (Veksler and Gov 2007):

$$F = \int \Big(\frac{1}{2}\kappa(H - \bar{H}n)^2 + (\sigma - \alpha n) + \gamma h^2 + k_B T n_s n(\ln(n) - 1) \Big)\, \mathrm{d}s, \tag{7}$$

where the first term gives the bending energy (Helfrich 1973) due to the mismatch between the membrane curvature and the spontaneous curvature of the PC. The second term describes the negative contribution of PCs (e.g. adhesion molecules) to the membrane surface tension. The third term gives the energy due to force of the cytoskeleton inside osteoblasts. The fourth term gives the entropic contribution due to the lateral thermal motion of the PC in the membrane in the limit of small n (Iglič et al. 2006). Here κ is the membrane bending constant (Helfrich 1973), H is the local mean membrane curvature, $\bar{H}$ is the intrinsic curvature of the PC, n is the area fraction of PCs, n_S is the saturation density of PCs on the membrane, σ is the membrane surface tension, α is a proportionality constant describing the effective interaction between the PCs and the external substrate, $h = h(x)$ describes the magnitudes of small deformations from the flat membrane, γ is a restoring spring constant and $\mathrm{d}s = d \cdot \mathrm{d}l$ is an element of membrane area, where d is the dimension of membrane perpendicular to the contour and $\mathrm{d}l$ is a line element along the contour. The local mean curvature is equal to $H = (\partial^2 y/\partial s^2)(\partial x/\partial s) - (\partial^2 x/\partial s^2)(\partial y/\partial s)$. The discretisation, $\mathrm{d}s$, equals $\sqrt{((\partial x/\partial s)^2 + (\partial y/\partial s)^2)}$.

Equation (7) is one-dimensional version of the more general expressions derived in Cai and Lubensky (1994) and Tu and Ou-Yang (2003). These expressions recover

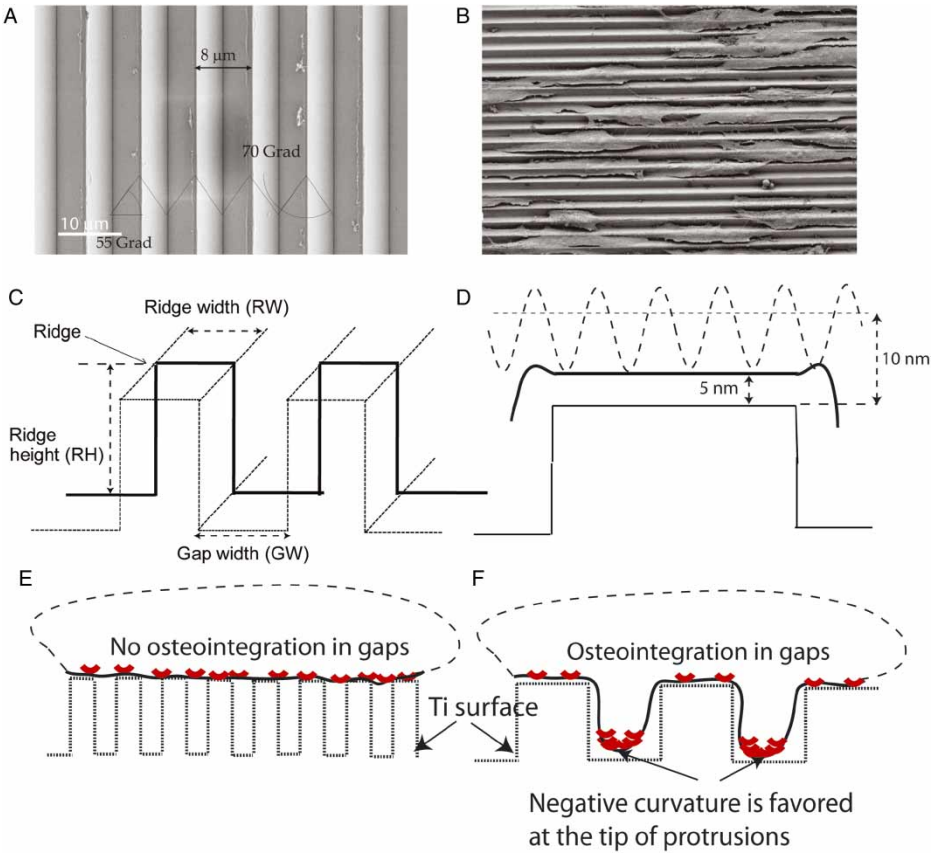

Figure 7. Schematic model of osteointegration growth along grooves of Ti surface. (A) Triangular profiles of Si wafer coated with a thin layer of Ti. The rills have an angle of 70 grd and a period of 8 μm. (B) Electron microscope image demonstrates how MG-63 osteoblast cells are growing along the triangular grooves. (C) The geometry of the Ti surface in our model. Due to translational symmetry, we model the osteoblast dynamics along the contour line of a longitudinal plane crossing the Ti surface ridges (bold line). Numerical simulations test the effects of varying the Ti surface RW, RH and GW. (D) The initial flattening of osteoblast membrane on top of a Ti surface ridge. The initial flat membrane shape (dotted line) is positioned 10-nm distance above the ridge surface line. Due to the instability between the density of adhesion molecules and the membrane shape, the small membrane protrusions grow crossing a threshold distance of 5 nm above the Ti surface (dashed line). Due to the strong electrostatic interactions, we assume that below this threshold distance, the membrane is then trapped and flattened to the end of the simulation (solid line), while the membrane away from the ridge is free to protrude between the grooves of Ti surface. (E) No osteointegration is expected in narrow grooves of Ti surface. Since the density of ridges is high, large numbers of adhesion molecules (bold crescents) are trapped and the growth in grooves is not facilitated. (F) Successful osteointegration is expected in wide grooves, since the numbers of adhesion molecules (bold crescents) are sufficient to allow growth in grooves.

the familiar form for small undulations of a flat membrane in the Monge approximation.

We next derive the equations of motions of the membrane contour using the variation of the free energy (Equation (7)) with respect to the membrane coordinate (Kabaso et al. 2010; Mark et al. 2010) and PC concentration (Kabaso et al. 2010). To take into account the drag due to viscous forces, we assume only local friction forces for simplicity (Veksler and Gov 2007; Kabaso et al. 2010), with coefficient ξ.

Before we give the equations of membrane motion, we should note that we assume that the membrane is nearly flat describing the length of a segment of the entire osteoblast cell. For the flat geometry, the equation of motion of the membrane is given by

$$\xi \frac{\partial \vec{r}}{\partial t} \cdot \vec{n} = -\frac{\delta F(s,t)}{\delta h}, \tag{8}$$

where $\vec{r}$ is the (x, y) coordinates, s is the contour length, t is time and $\vec{n}$ is the normal direction. Note that the force $\delta F(s,t)/\delta h$ equals the membrane shape velocity times friction coefficient, but opposite in direction. Since the relative change in the y direction (i.e. vertical) is greater than the change along the x-direction (i.e. horizontal), we only consider the changes along the y-direction. This simplification is, in fact, a variation of the Monge implementation, where the forces are applied along the vertical direction. In our case, it is satisfactory,

since we limit the change along the y-direction not to exceed a maximum ridge height (RH) ($<0.2\,\mu$m). Due to these reasons, the results will remain qualitatively the same neglecting the nonlinear term $(1/2)H^3$ in Equation (9).

In the free energy, we use a non-zero spring term to prevent drift due to the activity of adhesion. The variation of the free energy is projected to give the forces normal to the membrane contour (Kabaso et al. 2010; Mark et al. 2010). We now list the forces derived from the variation of the free energy (Equation (7)) (Kabaso et al. 2010; Mark et al. 2010):

$$F_{\text{curvature}} = \kappa\left(-\nabla^2 H + \bar{H}\nabla^2 n + \frac{1}{2}n^2\bar{H}^2 H - \frac{1}{2}H^3\right), \quad (9)$$

$$F_{\text{tension}} = (\sigma - \alpha n)H, \quad (10)$$

$$F_{\text{spring}} = -2\gamma y, \quad (11)$$

$$F_{\text{entropy}} = kTn_{\text{s}}(n\ln n - 1)H, \quad (12)$$

where $F_{\text{curvature}}$ is the force due to the curvature energy mismatch between the membrane curvature and the spontaneous curvature of the PCs, F_{tension} is the membrane tension force, F_{spring} is the spring restoring force and F_{entropy} arises from the entropy of the PCs in the membrane, which acts to expand the length of the contour. In order to control the growth of the cell contour length, we made use of a nonlinear form for the effective membrane tension:

$$\sigma = \sigma_0 \exp[\beta(L_{\text{t}} - L_{\text{init}})], \quad (13)$$

where L_{t} is the contour length, L_{init} is the initial contour length and β is the factor that determines the length scale at which the nonlinear growth in the tension sets in. Finally, the strong electrostatic interactions trap the membrane and prevent their further evolution throughout the simulation. This trapping occurs below a threshold distance of 5 nm.

We now calculate the dynamics of the PC density using the following conservation equation:

$$\frac{\partial n}{\partial t} = -\nabla\cdot\vec{J} = \frac{\Lambda}{n_{\text{s}}}\nabla\left(n\nabla\frac{\delta F}{\delta n}\right) - \frac{n}{\mathrm{d}l}\frac{\partial \mathrm{d}l}{\partial t}, \quad (14)$$

where Λ is the mobility of filaments and $\vec{J}$ is the total current of PC on the membrane, which includes the following terms:

$$J_{\text{attraction}} = \frac{\kappa\Lambda\bar{H}}{n_{\text{s}}}n\nabla H, \quad (15)$$

$$J_{\text{dispersion}} = -\frac{\kappa\Lambda\bar{H}^2}{n_{\text{s}}}n\nabla n, \quad (16)$$

$$J_{\text{diffusion}} = -D\nabla n, \quad (17)$$

where $J_{\text{attraction}}$ is the attraction flux resulting from the interaction between the PCs through the membrane curvature, $J_{\text{dispersion}}$ is the dispersion flux due to the membrane resistance to PC aggregation due to their membrane bending effects and $J_{\text{diffusion}}$ is the usual thermal diffusion flux, which depends on the diffusion coefficient, $D = \Lambda kT$. The last term in Equation (14) arises from the covariant derivative of the density with time on a contour whose length evolves with time. In this term $\mathrm{d}l$ is simply the line element. This term ensures that the total number of PC is conserved as the contour length changes.

4.3 Linear stability analysis

We next performed a linear stability analysis of the flat membrane model, as was previously done in Veksler and Gov (2007). The contour is allowed to evolve only along one direction, and we label the amplitude of the membrane fluctuation as $h(x)$, where x is the coordinate along the initial contour length. The curvature is linearised to be $H \simeq \nabla^2 h$, and the length element of the contour $\mathrm{d}l$ is given by $\mathrm{d}l = 1 + (\nabla h)^2/2$. Using this linearisation and linearising the equations of motion (Equations (8) and (14)), we then apply Fourier transform to get a 2×2 matrix whose eigenvalues give the dynamic evolution of small fluctuations from the equilibrium flat state. Both eigenvalues are real, and one of them is always negative and therefore represents only damped modes. The second solution can become positive in a range of wave vectors, representing unstable modes that grow with time. The following is the list of parameter values incorporated in the dispersion relation and numerical simulations: $\xi = 125\,\mathrm{s}^{-1}\,\mathrm{gr}$, $D_1 = 0.002\,\mu\mathrm{m}^2\,\mathrm{s}^{-1}$, $\alpha = 0.013\,\mathrm{gr\,s}^{-2}$, $\gamma = 0.00004\,\mathrm{gr\,s}^{-2}$, $n_{\text{s}} = 10\,\mu\mathrm{m}^{-2}$, $\kappa = 100\,kT$, $\bar{H} = -10\,\mu\mathrm{m}^{-1}$ and $\sigma = 0.001\,\mathrm{gr\,s}^{-2}$ (Simson et al. 1998). According to a typical diameter of an osteoblast cell, the initial length of the nearly flat modelled membrane is 15 μm. The total number of molecules remains fixed throughout the simulation. The total number of molecules is the total length of the modelled membrane (15 μm) times the average fractional density (0.1) divided by the length of a typical PC (10 nm) to give 150 molecules. The initial conditions of PCs are a uniform distribution of density 0.1 with small (1% of the maximum amplitude) random noise.

The flat membrane shape is initially positioned in 10 nm above the Ti ridge height (RH) (Figure 7).

There are two sources of dynamical instability: the first source originates from the mismatch between the spontaneous curvature of PCs and the membrane curvature, and the second source is due to adhesion forces which effectively reduce the membrane tension. The result of this dynamical instability is a dispersion relation of eigen values $w(q)$ obtained from the above-mentioned matrix. This dispersion relation has a non-stable region engulfed by two stable regions. In a non-stable region, a small perturbation (e.g. $<1\%$) is sufficient to initiate exponential growth, while a small perturbation in a stable region will decay exponentially. When the initial conditions are in the non-stable region, the growing membrane protrusions coalesce into a single pointed peak. At this region, the filament density is considerably greater than its initial density. In addition, the distribution of PCs matches the distribution of convex regions along the nearly flat membrane shape (Figure 6). This result is due to the attraction of PCs to convex regions (with negative curvature) that match their intrinsic spontaneous curvature of $-10\,\mu m^{-1}$.

4.4 *The effects of Ti surface shape on osteointegration*

Previous experimental studies have shown that osteoblasts do not grow in narrow grooves of the Ti implant surface,

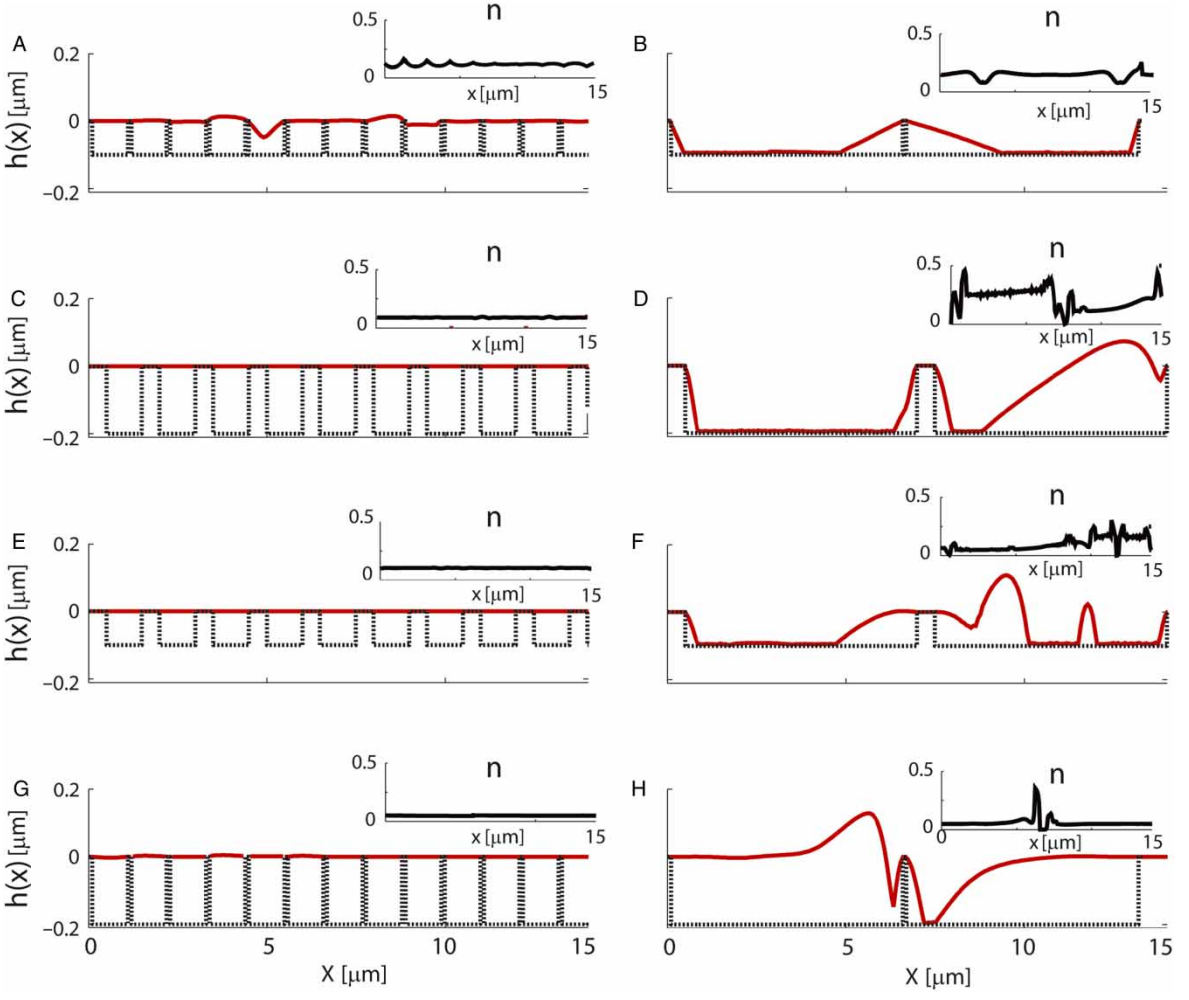

Figure 8. The effects of varying the RW, RH and GW on osteointegration. Each panel shows the osteoblast shape growth ($h(x)$; solid line) over the Ti surface (dotted line). Each inset shows the distribution of adhesion molecules (n; intrinsic curvature, $\bar{H} = -10\,\mu m^{-1}$) projected along the x-dimension of the Ti surface. The steady state time of the membrane shape ranges between 300 and 1000 s. The analysis of the Ti surface shape includes changes in the GW, RH and RW. The osteoblast growth is determined for a GW of 1 μm (A,C,E,G) vs. 6.5 μm (B,D,F,H), a RH of 0.1 μm (A,B,E,F) vs. 0.2 μm (C,D,G,H) and a RW of 0.5 μm (A,B,G,H) vs. 2 μm (C–F). Due to strong electrostatic interactions between the osteoblast shape and the Ti surface, we take into account an adhesion zone of 5-nm strip thickness above the Ti surface. Note the large growth seen in grooves of 6.5 μm vs. little growth seen along a GW of 1 μm. In these simulations the bending constant, $\kappa = 100\,kT$.

while successful growth is observed in wide grooves. The present model evaluates the functional effects on osteointegration by varying the three morphologic parameters of Ti surface shape, i.e. the groove width (GW), the ridge height (RH) and the ridge width (RW) (Figures 7 and 8). In addition, we will lower the energy cost of bending by reducing κ in Equation (7) demonstrating that the osteoblast can then grow in narrow grooves. The dynamics of membrane shape includes electrostatic interactions (at small length scale <5 nm) and dynamic instability due to adhesive forces (at large length scale >5 nm). The strong electrostatic interactions pin the membrane locally and prevent its further evolution with time. In fact, the membrane coordinates that come across this adhesion zone at <5 nm distance from the Ti surface will remain fixed to the end of the simulation (Figure 7). Note that this adhesion zone is expected to increase the stability in the system. On the other hand, the growth of membrane protrusions between the Ti surface grooves is driven by an instability due to a large adhesive strength, which effectively reduces the membrane tension (Figure 8). Our analysis reveals that the morphologic parameter that has the largest effect on osteoblast integration is the GW. In particular, Figure 8 demonstrates that over a GW of 6.5 μm, the osteointegration is greater than in narrow grooves of 1 μm. The RW also plays a crucial role determining the amounts of strong electrostatic interactions which pin the membrane and increase the membrane stiffness. In addition, less osteointegration is observed for a RW of 0.5 μm (second and third rows) in comparison to a RW of 0.1 μm (first and fourth rows). As predicted from the theory, we find that the distribution of PCs follows the membrane shape dynamics, where at regions of osteointegration, there is a large aggregation of adhesion molecules. To determine the role of the bending constant, we compared the osteoblast protrusion in 3 μm grooves for different values of κ (not shown). Results of these simulations reveal that the osteoblast protrusion in narrow grooves was considerable only for the lower bending constant, demonstrating the important role of bending energy to the success of osteointegration.

To have a better understanding of the underlying biophysical mechanisms allowing osteointegration only in wide grooves, we determined the contributions of fluxes due to PC spontaneous curvature to osteointegration. Numerical simulations revealed that the distribution of PCs followed the distribution of membrane curvature. At protrusive regions, the density of PCs and the fluxes due to membrane curvature are high. On the other hand, since the membrane regions above the ridge surface were nearly flat, the fluxes due to membrane curvature were diminished. While the relative contributions of fluxes due to diffusion were minor, the PC density at these regions was close to the initial value, n_0. Therefore, the ridge region poses an energy barrier over which the PCs cannot cross through, and the remaining number of PCs in the narrow grooves is not sufficient for successful osteointegration.

5. The effects of Ti surface pillar width

A different type of Ti surface geometry is the osteoblast growth along Ti surface pillars rather than ridges. Electron microscope images of osteoblasts grown on a triangular groove (Figure 7(A,B)) and on a pillar Ti surface (Figure 9(A1,2)) reveal considerable differences in osteointegration. The reference cells grown on a planar surface attach their entire cell body to the surface, whereas cells grown on a pillar surface adhere exclusively to the top of pillars while sending filopods to the bottom surface. Furthermore, confocal microscope images reveal the accumulation of short actin fibres at the top of the pillars (Figure 9(A4)), while the osteoblast growth on a triangular Ti surface forms long actin fibres (Figure 9(A3)). Previously, it was indicated that PCs with negative intrinsic curvature are bound to actin filaments at the leading convex edge of a growing membrane. However, the fragmentation of actin filaments and PCs along a concave membrane shape at the top of pillars will increase the membrane tension. To investigate the contribution of pillar width on the induced membrane tension, we modelled the distribution of PCs along the observed invagination regions on the top of a narrow (Figure 9(C,D)) and a wide (Figure 9(E,F)) pillar. We found that on top of a narrow pillar, the concavity region is greater leading to stronger depletion of PCs than observed on a wide pillar. This depletion will increase the membrane surface tension built on top of pillars, due to the binding of PCs to the fragmented actin filaments.

6. Conclusions and discussion

In accordance with the previous suggestions (Smith et al. 2004; Puckett et al. 2008; Smeets et al. 2009), we have shown that positively charged proteins attached to the negatively charged implant surface can mediate the adhesion of negatively charged osteoblasts to negatively charged Ti surface. As shown in Figure 2, the protein adsorption to the implant surface may be driven by electrostatic interactions between the positive sites of the protein and the negative implant surface (MacDonald et al. 1998). Another possible or additional explanation of adsorption of charged proteins on the Ti implant surface may include also the monovalent and divalent salt bridges (Ellingsen 1991; Yang et al. 2003). We also investigated how the mediated protein adsorption and strong electrostatic interactions with the Ti implant may affect the

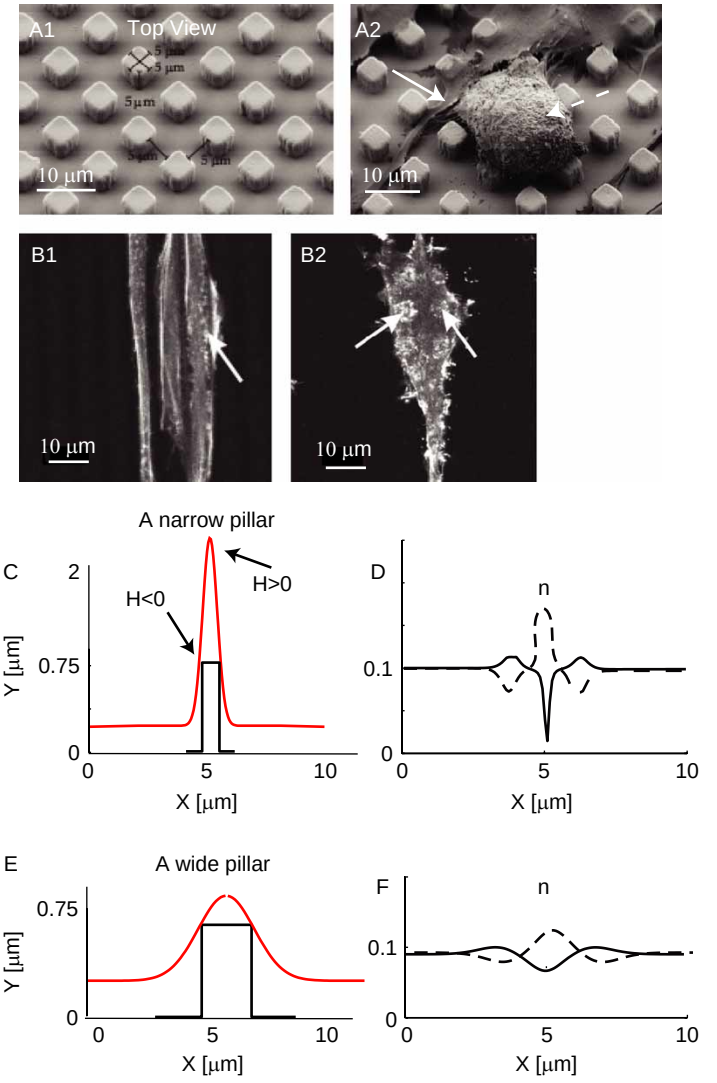

Figure 9. The effects of the Ti pillar width on the distribution of PCs. (A1) Arrays of cubic pillars with vertical side walls of 5 μm length are obtained using a photolithographic process on a Si wafer. The structured surface array is coated with Ti of approximately 100-nm thickness. (A2) Electron microscope images of human osteoblasts on Ti surface pillars demonstrate that the membrane growth is more in between than on top of pillars (white arrow). Note how the cell body of a second cell (dashed arrow) sends filopods. Confocal images of human osteoblast cells along triangular grooves (B1; for structure see Figure 7(A)) and pillars (B2; for structure see A1) of structure Ti surfaces. It is shown that on a triangular Ti surface, the actin is organised in well-defined long actin fibres, whereas on a pillar surface, the actin fibres are more fragmented accumulating on top of each pillar (white arrows). We compare the dynamics of PCs of negative intrinsic curvature ($\bar{H} = -10\,\mu\text{m}^{-1}$) near a narrow (C and D) and a wide (E and F) pillar. Note that the curved membrane is composed of both positive curvature (at the tip) and negative curvature regions (at the sides of each pillar). Starting from an initial uniform distribution of PCs ($n_0 = 0.1$), the PCs are attracted to negative curvature region and are repelled from positive curvature regions (solid lines). On the other hand, since actin filaments are linked to the PCs, the predicted distribution of PCs is mainly at the top of pillars (dashed lines). Note that both types of pillars are of the same height and that the membrane shape is fixed during the simulation.

dynamics of osteointegration at greater distance from the implant.

The adhesion of osteoblast-like cells (i.e. bone cells) to a Ti surface implant is a dynamic process driven by the interaction with the extracellular matrix as well as intracellular mechanisms. It has been shown that the adhesion to the extracellular matrix mediates the transport of curvature inducing adhesion molecules to the membrane thereby relieving the surface membrane tension and allowing membrane protrusive growth (Veksler and Gov 2007; Kabaso et al. 2010).

In addition, the membrane protrusive growth is also mediated by positive feedback between the curvature inducing molecules (e.g. IRSp53 and fibronectin) and the membrane curvature. While the above-mentioned mechanisms increase the instability in our system, the strong adhesion to the Ti surface due to electrostatic interactions will increase the system stability as well as the membrane

surface tension. In recent theoretical studies, the use of an external actin nucleation force was coupled to the density of PCs (Veksler and Gov 2007). Since the nucleation of actin was mainly at membrane regions of high PC density, this mechanism can also be applied to explain the growth of membrane protrusions in between Ti surface ridges.

In the first set of presented biomechanical simulations, we investigate the initial membrane protrusive growth over a ridge-like Ti surface pattern with three morphologic features, the ridge height (RH), the ridge width (RW) and the inter-distance between ridges (i.e. denoted as the GW). Since the ridge top surface is planar, the membrane growth against it will flatten its growing tips. We also assume that due to strong electrostatic interactions, the flatten membrane is trapped to the end of a simulation. As a result, the fluxes of PCs due to curvature are diminished and surface membrane tension is increased at the convex regions of a ridge. To conclude the interplay between the sources of stability and instability can help us to determine the optimal topography of a Ti surface implant.

To evaluate how the osteointegration is affected along grooves on a Ti surface, we varied the RH, the RW and the inter-distance between ridges (i.e. the GW). Results of simulations reveal that the GW has the largest impact on osteointegration. In fact, the membrane along a wide groove is longer, having more PCs than the membrane along a narrow groove. Consequently, it can drive the growth of filopodia-like protrusions. On the other hand, a high ratio of RW over GW will increase the size of trapped and flatten membrane regions, which will reduce the amounts of available PCs needed for the success of osteointegration. Therefore, we suggest that a wide groove contributes to the instability, while a high and wide ridge contributes to the stability in our system.

To isolate the contribution of the bending modulus, simulation results reveal that by lowering of the bending modulus κ, the osteointegration in relatively narrow grooves (3 μm) was increased in comparison to a reference bending modulus. This shows that in a plausible range of κ, the results of simulations may change considerably demonstrating the important contribution of the bending energy to osteointegration.

At a later stage of osteointegration, the bounded regions on top of Ti surface ridges and pillars may form focal adhesions. In a recent experimental study, fragmented actin fibres were observed at the top of Ti surface pillars. Since actin fibres have also been shown to bind adhesion molecules of negative inducing curvature (e.g. IRSp53) (Mattila et al. 2007), we suggest here the co-localisation of adhesion molecules on top of pillars. This co-localisation is not favourable, since at the top of pillars the membrane curvature is positive. The investigation of the effects of the pillar width on the distribution of PCs reveals a disagreement between their calculated distribution, obtained from their linkage to the fragmented actin filaments, to the preferred distribution according to the negative intrinsic curvature of PCs. We find that the preferred one was to the side regions of the pillar (towards the convex membrane regions), while the predicted distribution is at the top of the pillars (towards the concave membrane regions). This disagreement is expected to increase locally the membrane surface tension, which increases the energy costs of lateral membrane expansion. This could also explain the preferred growth of osteoblast cells towards the bottom of triangular grooves (Figure 7(B)).

The main result of the biomechanical part of our study is that the decreased width of the grooves results in a decreased adhesion and ingrowth between the grooves, which is supported by various experimental studies (Puckett et al. 2008; Lange et al. 2009; Lamers et al. 2010; Matschegewski et al. 2010). Puckett et al. (2008) have shown that the decrease in the width of nanorough regions (of dimension from 80 to 22 μm and 48 to 22 μm) resulted in significant reductions in the number of osteoblast cells adhering to the structured surface. One explanation is that due to their large cell size (20–30 μm in length), osteoblast cells are unable to fit their entire length into a narrow groove without membrane bending. Results in this study reveal that the observed reduction in cell adhesion can be indeed due to high-bending energy, which reduces the osteointegration in between narrow grooves.

In Puckett et al. (2008), osteoblast morphology in the smallest nanorough region (22 μm) was more round and had less diffuse F-actin filaments, while filopods extending from the cells remained near their origin. It was hypothesised that osteoblasts recognise different surface roughness through the interaction of proteins in the extracellular matrix. In other study (Lamers et al. 2010), it was even shown that osteoblasts are responsive to nanopatterns of smaller length scale below 100 nm in GW and depth, which was detected by the deposition of minerals (e.g. hydroxypatite) along nanosize patterns. Finally, a recent work by Matschegewski et al. (2010) revealed that on top of pillars in a cubic-structured Ti surface, the actin filaments were more fragmented and short in comparison to long actin filaments observed in reference cells grown on a smooth surface. This study suggests that the aggregation of short actin filaments on top of pillars is due to strong electrostatic interactions at the top surface of the pillars. In addition, the flattening of the cell membrane during growth against the top surface of a pillar may prevent the diffusion of curvature-induced fluxes of PCS, which then prevents the growth of membrane extensions from the membrane regions near the pillar. As a result, the mismatch in the curvature bending energy of PCs is not relieved and the cell becomes more round.

Considering the findings in this study, we suggest the ratio of RW over GW as the critical morphologic parameter (i.e. $F_c = RW/GW$, see also Figure 7) which determines the efficiency of initial osteointegration in between ridges (Figure 7). For example, when this ratio was 0.08 (Figure 8(B)), long membrane protrusions were formed, while very short filopods were observed for a ratio of 0.5 (Figure 8(E)). To obtain information about the relative contribution of each of the energy terms in Equation (7) to the total bending energy, each term was normalised by the total bending energy, while this normalisation is performed at the maximum membrane bending location. It is shown that for the case of $F_c = 0.08$, the contribution of the first term, i.e. the curvature mismatch energy term, was 0.8, while the spring and tension energy terms were 0.17 and 0.01, respectively. For the case of $F_c = 0.5$, the curvature mismatch energy term was 0.43, while the tension energy term was 0.42. In fact, the tension energy term was indeed greater for the smallest critical ratio F_c in comparison to the largest ratio.

To conclude, the present study demonstrated how positively charged proteins mediate the adhesion of negatively charged osteoblasts to negatively charged implant surface. In addition to this mathematical analysis, a dynamical model investigated the contribution of the bending energy of an initially nearly flat membrane to the ingrowth of filopodia-like protrusion between Ti surface ridges. We showed that the strong electrostatic binding of the cell membrane to the Ti surface effectively sequester the PCs from driving the membrane ingrowth away from the bounded regions. In addition, the success of osteointegration between grooves depended on the GW. In particular, the bending energy involved in folding the cell membrane along a narrow groove was too high to be compensated by the reduced membrane tension mediated by the adhesion of the osteoblast cell to the extracellular matrix. Finally, it remains to be tested how the bending of the entire osteoblast cell is affected by the implant surface pattern and how it will affect the cell alignment, cell orientation and cell motility.

Acknowledgements

This work was supported by ARRS grants J3-9219-0381, P2-0232-1538 and DFG for the project A3 in Research Training Group 1505/1 '*welisa*'. The authors thank Nir Gov for helpful discussion.

References

Bohinc K, Slivnik T, Iglič A, Kralj-Iglič V. 2008. Advances in planar lipid bilayers and liposomes. Vol. 8. San Diego (CA): Elsevier Academic Press. Chapter 4. Membrane electrostatics – a statistical mechanical approach to the functional density theory of electric double layer. p. 107–154.

Brock A, Chang E, Ho CC, LeDuc P, Jiang X, Whitesides GM, Ingber DE. 2003. Geometric determinants of directional cell motility revealed using microcontact printing. Langmuir. 19(5):1611–1617.

Butt HJ, Graf K, Kappl M. 2003. Physics and chemistry of interfaces. 1st ed. Weinheim: Wiley.

Cai W, Lubensky TC. 1994. Covariant hydrodynamics of fluid membranes. Phys Rev Lett. 73(8):1186–1189.

Cai K, Frant M, Bossert J, Hildebrand G, Liefeith K, Jandt KD. 2006. Surface functionalized titanium thin films: zeta-potential, protein adsorption and cell proliferation. Coll Surf B. 50(1):1–8.

Cevc G. 1990. Membrane electrostatics. Biochim Biophys Acta. 1031(3):311–382.

Chapman DL. 1913. A contribution to the theory of electrocapillarity. Philos Mag. 25(148):475–481.

Discher DE, Janmey P, Wang YL. 2005. Tissue cells feel and respond to the stiffness of their substrate. Science. 310(5751):1139–1143.

Ellingsen JE. 1991. A study on the mechanism of protein adsorption to TiO_2. Biomaterials. 12(6):593–596.

Engler A, Bacakova L, Newman C, Hategan A, Griffin M, Discher D. 2004. Substrate compliance versus ligand density in cell on gel responses. Biophys J. 86(1):617–628.

Frenkel D, Smith B. 2002. Understanding molecular simulation from algorithms to applications. London: Academic press.

Gouy MG. 1910. Sur la constitution de la charge electrique a la surface d'un electrolyte. J Phys. (France). 9(1):457–468.

Helfrich W. 1973. Elastic properties of lipid bilayers: theory and possible experiments. Z Naturforsch C. 28(11):693–703.

Iglič A, Brumen M, Svetina S. 1997. Determination of inner surface potential of erythrocyte membrane. Bioelectrochem Bioenerg. 43(1):97–103.

Iglič A, Slivnik T, Kralj-Iglič V. 2007. Elastic properties of biological membranes influenced by attached proteins. J Biomech. 40(11):2492–2500.

Iglič A, Hägerstrand H, Veranič P, Plemenitaš A, Kralj-Iglič V. 2006. Curvature induced accumulation of anisotropic membrane components and raft formation in cylindrical membrane protrusions. J Theor Biol. 240(3):368–373.

Iglič A, Lokar M, Babnik B, Slivnik T, Veranič P, Hägerstrand H, Kralj-Iglič V. 2007. Possible role of flexible red blood cell membrane nanodomains in the growth and stability of membrane nanotubes. Blood Cells Mol Dis. 39(1):14–23.

Israelachvili JN. 1997. Intermolecular and surface forces. London: Academic Press.

Kabaso D, Shlomovitz R, Auth T, Lew LV, Gov NS. 2010. Curling and local shape changes of red blood cell membranes driven by cytoskeletal reorganization. Biophys J. 99(3): 808–816.

Lamers E, Walboomers XF, Domanski M, te Riet J, van Delft FC, Luttge R, Winnubst LA, Gardeniers HJ, Jansen JA. 2010. The influence of nanoscale grooved substrates on osteoblast behavior and extracellular matrix deposition. Biomaterials. 31(12):3307–3316.

Lange R, Elter P, Matschegewski C, Weidmann A, Löffler R, Fleischer M, Nebe JB, Kern D, Beck U. 2009. Material and cell biological investigations on structured biomaterial surfaces with regular geometry. Proceedings of the 3rd International Symposium Interface Biology of Implants; Rostock, Germany.

MacDonald DE, Markovic B, Boskey AL, Somasundaran P. 1998. Physico-chemical properties of human plasma fibronectin binding to well characterized titanium dioxide. Coll Surf B. 11(3):131–139.

Mark S, Shlomovitz R, Gov NS, Poujade M, Grasland-Mongrain E, Silberzan P. 2010. Physical model of the dynamic instability in an expanding cell culture. Biophys J. 98(3): 361–370.

Matschegewski C, Staehlke S, Loeffler R, Lange R, Chai F, Kern DP, Beck U, Nebe BJ. 2010. Cell architecture–cell function dependencies on titanium arrays with regular geometry. Biomaterials. 31(22):5729–5740.

Mattila PK, Pykalainen A, Saarikangas J, Paavilainen VO, Vihinen H, Jokitalo E, Lappalainen P. 2007. Missing-in-metastasis and IRSp53 deform PI(4,5)P2-rich membranes by an inverse BAR domain-like mechanism. J Cell Biol. 176(7): 953–964.

Monsees TK, Barth K, Tippelt S, Heidel K, Gorbunov A, Pompe W, Funk RHW. 2005. Surface patterning on adhesion, differentiation, and orientation of osteoblast-like cells. Cells Tissues Organs. 180(2):81–95.

Moreira AG, Netz RR. 2002. Simulations of counterions at charged plates. Eur Phys J E. 8(1):33–58.

Oghaki M, Kizuki T, Katsura M, Yamashita K. 2001. Manipulation of selective cell adhesion and growth by surface charges of electrically polarized hydroxyapatite. J Biomed Mater Res. 57(3):366–373.

Peter BJ, Kent HM, Mills IG, Vallis Y, Butler PJ, Evans PR, McMahon HT. 2004. BAR domains as sensors of membrane curvature: the amphiphysin BAR structure. Science. 303(5657):495–499.

Perutkova Š, Frank M, Bohinc K, Bobojevic G, Rozman B, Kralj-Iglic V, Iglic A. 2010. Interaction between equally charged membrane surfaces mediated by positively and negatively charged macroions. J Membr Biol. 236(1):43–53.

Perutkova Š, Kralj-Iglič V, Frank M, Iglič A. 2010. Mechanical stability of membrane nanotubular protrusions influenced by attachment of flexible rod-like proteins. J Biomech. 43(8): 1612–1617.

Puckett S, Pareta R, Webster TJ. 2008. Nano rough micron patterned titanium for directing osteoblast morphology and adhesion. Int J Nanomed. 3(2):229–241.

Roessler S, Zimmermann R, Scharnweber D, Werner C, Worch H. 2002. Characterization of oxide layers on Ti6Al4V and titanium by streaming potential and streaming current measurements. Coll Surf B. 26(4):387–395.

Safran S. 1994. Statistical thermodynamics of surfaces, interfaces, and membranes. Reading (MA): Addison-Wesley Publishing Company.

Shlomovitz R, Gov NS. 2008. Physical model of contractile ring initiation in dividing cells. Biophys J. 94(4):1155–1168.

Simson R, Wallraff E, Faix J, Niewohner J, Gerisch G, Sackmann E. 1998. Membrane bending modulus and adhesion energy of wild-type and mutant cells of dictyostelium lacking talin or cortexillins. Biophys J. 74(1):514–522.

Sorre B, Callan-Jones A, Manneville JB, Nassoy P, Joanny JF, Prost J, Goud B, Bassereau P. 2009. Curvature-driven lipid sorting needs proximity to a demixing point and is aided by proteins. Proc Natl Acad Sci. 106(14):5622–5626.

Smeets R, Kolk A, Gerressen M, Driemel O, Maciejewski O, Hermanns-Sachweh B, Riediger D, Stein JM. 2009. A new biphasic osteoinductive calcium composite material with a negative zeta potential for bone augmentation. Head Face Med. 5:13, doi: 10.1186/1746-160X-5-13.

Smith IO, Baumann MJ, McCabe LR. 2004. Electrostatic interactions as a predictor for osteoblast attachment to biomaterials. J Biomed Mater Res A. 70(3):436–441.

Teng NC, Nakamura S, Takagi Y, Yamashita Y, Ohgaki M, Yamashita K. 2000. A new approach to enhancement of bone formation by electrically polarized hydroxyapatite. J Dent Res. 80(10):1925–1929.

Tu ZC, Ou-Yang ZC. 2003. Lipid membranes with free edges. Phys Rev E. 68(6 Pt 1):061915.

Urbanija J, Bohinc K, Bellen A, Maset S, Iglic A, Kralj-Iglic V, Sunil Kumar PBS. 2008. Attraction between negatively charged surfaces mediated by spherical counterions with quadrupolar charge distribution. J Chem Phys. 129(10): 105101.

Veksler A, Gov NS. 2007. Phase transitions of the coupled membrane-cytoskeleton modify cellular shape. Biophys J. 93(11):3798–3810.

Walboomers FF, Jansen JA. 2001. Cell and tissue behaviour on micro-grooved surface. Odontology. 89(1):2–11.

Yang Y, Glover R, Ong JL. 2003. Fibronectin adsorption on titanium surfaces and its effect on osteoblast precursor cell attachment. Coll Surf B. 30(4):291–297.

Zimmerberg YJ, Kozlov MM. 2006. How proteins produce cellular curvature. Nat Rev Mol Cell Biol. 7(1):9–19.